The sources of deep ocean infragravity waves observed in the North Atlantic Ocean

4 authors, including:

Wayne C Crawford
Institut de Physique du Globe de Paris

67 PUBLICATIONS   **1,014** CITATIONS

SEE PROFILE

X. Bertin
Université de La Rochelle

98 PUBLICATIONS   **935** CITATIONS

SEE PROFILE

RESEARCH ARTICLE

Key Points:
- Two midlatitude coastal regions dominate deep North Atlantic Ocean IG wave generation
- The source parameters are weaker in the source regions than they are at higher latitudes
- Site characteristics appear to be more important than absolute source levels

Supporting Information:
- Supporting Information S1
- Movie S1

Correspondence to:
W. Crawford,
crawford@ipgp.fr

The sources of deep ocean infragravity waves observed in the North Atlantic Ocean

Wayne Crawford[1], Valerie Ballu[2], Xavier Bertin[2], and Mikhail Karpytchev[2]

[1]Institut de Physique du Globe de Paris, Sorbonne Paris Cité, Université Paris Diderot, UMR 7154 CNRS, Paris, France, [2]UMR 7266 LIENSs CNRS-Université de La Rochelle, La Rochelle, France

Abstract Infragravity waves are long-period (25–250 s) ocean surface gravity waves generated in coastal zones through wave-wave interactions or oscillation of the breaking point. Most of the infragravity wave energy is trapped or dissipated near coastlines, but a small percentage escapes into the open oceans. The source of deep ocean infragravity waves is debated, specifically whether they come mostly from regions with strong source waves or from sites with particular morphologies/orientations. We correlate measurements of infragravity waves in the deep North Atlantic Ocean with infragravity wave generation parameters throughout the Atlantic Ocean to find the dominant sources of deep ocean infragravity wave energy in the North Atlantic Ocean. The deep ocean infragravity wave data are from a 5 year deployment of absolute pressure gauges west of the Azores islands (37°N, 35°W) and shorter data sets from seafloor tsunami gauges (DART buoys). Two main sources are identified: one off of the west coast of southern Europe and northern Africa (25°N–40°N) in northern hemisphere winter and the other off the west coast of equatorial Africa (the Gulf of Guinea) in southern hemisphere winter. These regions have relatively weak source waves and weak infragravity wave propagation paths to the main measurement site, indicating that that the site morphology/orientation dominates the creation of deep ocean infragravity waves. Both regions have also been identified as potential sources of global seismological noise, suggesting that the same mechanisms may be behind the generation of deep ocean infragravity waves and global seismological noise in the frequency band from 0.001 to 0.04 Hz.

1. Introduction

Oceanic infragravity waves (hereafter, "IG waves") are ocean surface gravity waves with periods from 25 to more than 250 s. Two main mechanisms are usually proposed to explain their generation: (1) the second-order nonlinear wave-wave interaction between wind waves [*Hasselmann*, 1962; *Longuet-Higgins and Stewart*, 1962; *Okihiro et al.*, 1992] and (2) the time-varying oscillation of the nearshore breaking point [*Symonds et al.*, 1982; *Baldock*, 2012; *Pomeroy et al.*, 2012]. The first mechanism was shown to dominate on gently sloping beaches due to the shoaling of the bound waves [*Herbers et al.*, 1995a], while the second mechanism occurs preferentially over steep bottoms [*Baldock*, 2012; *Pomeroy et al.*, 2012]. When depth-limited breaking of short waves occurs in the nearshore, IG waves can be released as linear surface gravity waves ("free" IG waves) [e.g., *Gallagher*, 1971; *Herbers et al.*, 1995a, 1995b]. IG waves are important in coastal sediment transport, can generate dangerous seiches in harbors [*Okihiro et al.*, 1993; *Rabinovich*, 2009; *Ardhuin et al.*, 2014], and may be the source of background-free oscillations of the earth [*Rhie and Romanowicz*, 2006; *Webb*, 2007; *Uchiyama and McWilliams*, 2008; *Webb*, 2008; *Fukao et al.*, 2010; *Traer et al.*, 2012; *Ardhuin and Herbers*, 2013].

Although most of the free IG wave energy is refractively trapped or dissipated at coastlines, some of the energy leaks into the deep ocean [*Munk et al.*, 1964; *van Dongeren and Svendsen*, 2000; *Thomson et al.*, 2007; *Dolenc et al.*, 2008; *Uchiyama and McWilliams*, 2008]. Once there, free IG waves can propagate across the ocean basin with little attenuation [e.g., *Snodgrass et al.*, 1966; *Shillington*, 1981]. They also create a seafloor pressure and acceleration signal that can both mask seismic wave arrivals [*Webb and Crawford*, 1999] and be used to determine the elastic properties of the underlying sediments and crust (the seafloor compliance method) [e.g., *Yamamoto and Torii*, 1986; *Crawford et al.*, 1991; *Zha et al.*, 2014]. Deep ocean IG waves may provoke ice shelf fracturing [*Bromirski et al.*, 2010] and hinder satellite determination of ocean currents [*Ardhuin et al.*, 2014]. Henceforth, when we discuss deep ocean IG waves, we are implicitly talking about free IG waves, as the bound waves are not detected at the seafloor [e.g., *Webb et al.*, 1991].

Understanding the source of deep ocean IG waves may be important for selecting appropriate windows for satellite measurements and for predicting the signal (noise) for seafloor compliance (seismology) measurements. *Webb et al.* [1991] compared deep seafloor IG wave signals at two sites: one in the northeast Pacific Ocean and the other in the northwest Atlantic Ocean. They found that the IG wave signal was much stronger and less variable at the Pacific Ocean site, which they explained as the result of the much longer source region (i.e., coastlines exposed to large/long swells and with direct raypaths to the site) in the Pacific Ocean. Recently, *Aucan and Ardhuin* [2013] performed a similar analysis using mainly data from DART tsunami gauges (http://www.ndbc.noaa.gov/dart/dart.shtml), which provide longer time series and better calibration than the differential pressure gauges used in the *Webb et al.* [1991] study. Using data from 32 Pacific Ocean sites and 6 North Atlantic Ocean sites, they determined that the energy and variability of IG wave signals in the Pacific Ocean were not significantly different from those in the North Atlantic Ocean.

Ardhuin et al. [2014] empirically determined that nearshore seafloor IG wave levels correlate well with the significant wave height (H_S) multiplied by the square of the energetic mean wave period $T_{m0,-2}$. *Rawat et al.* [2014] used a spectral wave model to propagate wave energy calculated from some large storms using this "IG wave generation parameter" to distant deep ocean sites, finding a good correlation with the measured IG wave levels. We ask the following question: Does deep ocean IG energy depend primarily on efficient IG wave propagation from areas with strong IG wave generation parameters? Or do other factors, such as the coastal morphology and the impinging wave direction, dominate the generation of deep ocean IG waves?

To address these questions, we calculated the correlation coefficient between deep ocean IG wave measurements made in the North Atlantic Ocean and IG wave generation parameters calculated using a wave numerical hindcast throughout the Atlantic Ocean, neighboring seas, and a portion of the Southern Ocean. The primary seafloor IG wave data set comes from a 5 year deployment of absolute pressure gauges on the Mid-Atlantic Ridge at 37°N, providing a longer time span and higher instrument precision than the publically available DART gauge data. We complement this data set with data from North Atlantic DART gauges, to evaluate the dependence of the correlations on the position of the deep ocean measurements.

2. Data Sources and Processing

Ardhuin et al. [2014] determined that IG wave heights are best correlated with the ocean surface wave height (H_S) multiplied by the mean or peak wave period squared. They found that the correlation was slightly better using the energetic mean wave period $T_{m0,-2}$ than with the peak wave period T_P, but the difference is small [*Rawat*, 2015]. In addition, T_P is a standard parameter that can be validated using buoy data [e.g., *Dodet et al.*, 2010], whereas $T_{m0,-2}$ implies extra computations based on wave spectra that are much less often available from buoy data. We therefore use $H_S * T_p^2$ as the surface IG wave generation parameter in this paper.

We calculate H_S and T_P^2 over the Atlantic Ocean and neighboring waters using a 0.5° grid from −69.5° to 69.5°N and −100°E to 20°E (Figure 1), using a wave numerical hindcast based on the spectral wave model WaveWatchIII (Version 3.14) [*Tolman, 2009*], which solves the wave action equation on regular grids using finite differences. The spectral space was discretized using 24 equally spaced directions and 36 frequencies spanning 0.036–1.01 Hz. Sea-ice was taken into account according to the procedure described in *Bertin et al.* [2013]. The source terms associated with wind input and dissipation by whitecapping were computed using the parameterization Cycle 4 described in *Bidlot et al.* [2007] and the model was forced with wind fields originating from the ERA-Interim reanalysis [*Dee et al., 2011*]. The model was run from 2007 to 2012 and fields of H_s and T_p were archived every 3 h over the whole domain.

We validated the model predictions against H_s data derived from altimeters, quality-controlled, and archived in the Globwave database (http://www.globwave.org). The data comparison (Figure 2) was performed following the methodology described in *Rascle et al.* [2008], where points located in water depth shallower than 50 m were removed from the computation because coastal zones are poorly represented with our 0.5° resolution and altimeter-derived H_S are also less accurate. This comparison reveals a Root Mean Square Error (RMSE) ranging from 0.10 to 0.80 m, yielding a 8–30% error once normalized by the data (NRMSE). Integrated over the whole domain, the mean bias is negligible (0.03 m), the RMSE is 0.40 m, and the NRMSE is 16%. RMSE between T_P and buoy data available in the NE Atlantic Ocean and used in *Dodet*
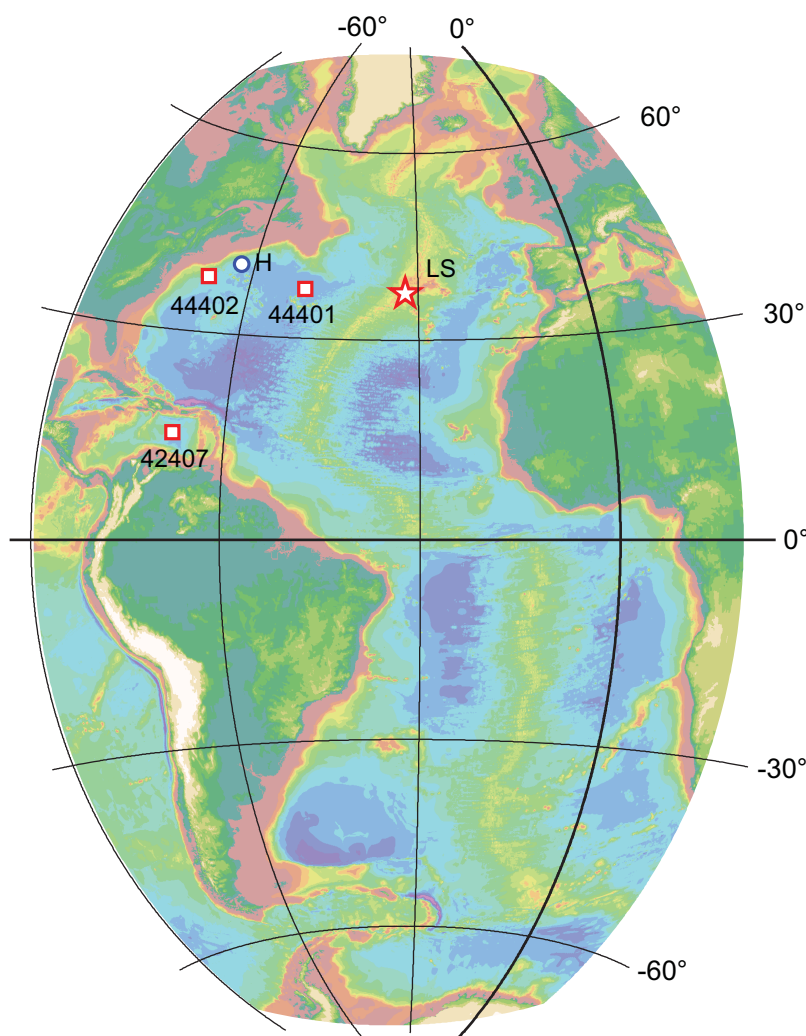
Figure 1. Map of the range of latitudes and longitudes over which we calculated wave heights and significant periods. Symbols = seafloor pressure sensor stations: LS = Lucky Strike; 44401, 44402, 42407 = DART buoys; H = HEBBLE site (not used in this paper, but used in *Webb et al.* [1991]).

et al. [2010] is of the order of 1–1.5 s. Recently developed parameterizations [e.g., *Rascle and Ardhuin*, 2013] give approximately 30% smaller error, but we consider that our hindcast is accurate enough for this study.

We calculated deep ocean IG waves levels using seafloor absolute pressure time series. Our primary data source is an observatory site on the Mid-Atlantic Ridge at 37°N, where we deployed absolute pressure gauges from 2007-present as part of the EMSO-MoMAR seafloor observatory around Lucky Strike volcano [*Cannat et al.*, 2011; *Colaço et al.*, 2011]. The pressure gauge deployment was part of a long-term study of vertical motions along the ridge segment [*Ballu et al.*, 2009]. We combined data from four overlapping deployments of Seabird SBE53 absolute pressure gauges, covering the period from July 2008 to May 2013. We also used data from DART (Deep ocean Assessment and Reporting of Tsunamis) buoys in the North Atlantic Ocean with data on or after 2007 that are publically available from the National Geophysical Data Center (NGDC: http://www.ngdc.noaa.gov/hazard/DARTData.shtml). Table 1 summarizes the sites and their date ranges.

We calculated the IG wave heights over these sites using absolute pressure data from which the tidal signal was removed. For the Lucky Strike data, we used a four-pole high-pass Butterworth filter with corner frequency at 10,000 s, whereas for the DART data we used detided data provided by the NGDC. We calculated 6 h power spectral densities (Pa²/Hz), each consisting of 25 overlapping 1000 s FFTs, then converted to $m/\sqrt{Hz}$ at the ocean surface using the ocean surface wave dispersion and pressure-depth relations [e.g., *Apel*, 1987]. Finally, we integrated these values over the frequency band from 0.006 to 0.01 mHz, where the
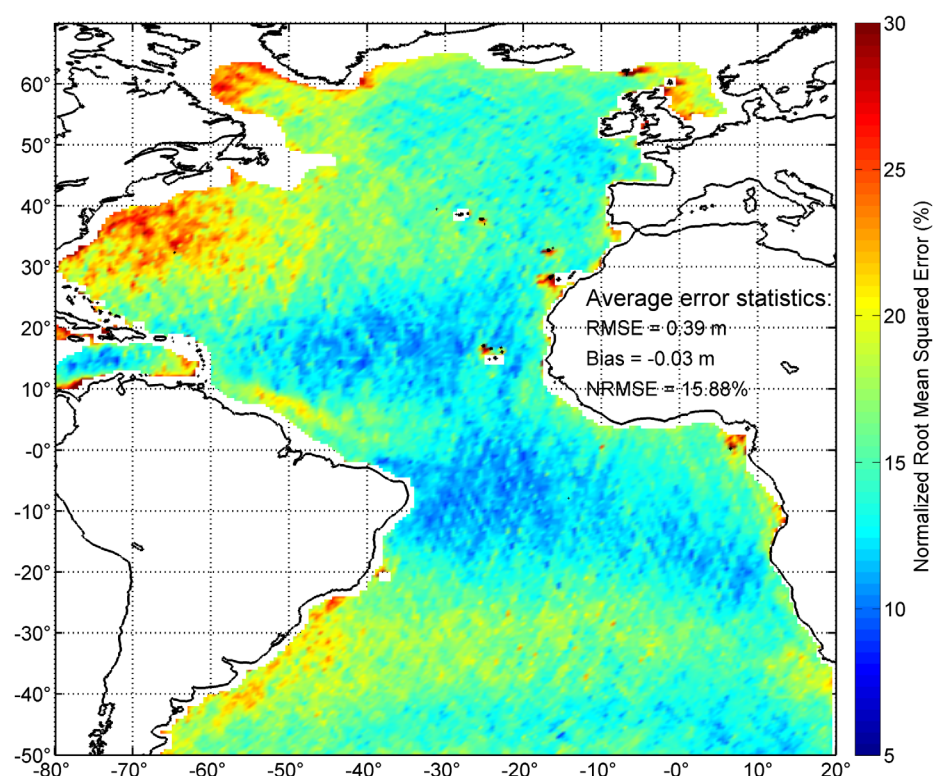
Figure 2. Normalized RMS Error (NRMSE) for modeled Hs over the Atlantic Ocean computed from 2007 to 2013 against H_S derived from altimeters ERS2, Jason-1, Jason-2 Geosat, Cryosat, and Envisat. The model NRMSE ranges from 5 to 25%, with a mean of 16%.

behavior of the spectra is clearly consistent with IG waves according to two criteria: (1) the shape of the pressure spectrum corresponds with that expected for a flat sea-surface IG wave spectrum under hydrody-namic depth filtering (Figure 3a), and (2) the correlation between two nearby gauges is consistent with that expected for ocean surface gravity waves [*Webb*, 1986] (Figure 3b). Above 0.01 Hz, the spectral shape is approximately correct but the correlations are not, whereas below 0.005–0.006 Hz the spectral levels rise rapidly with decreasing frequency. We use these average 6 h IG wave heights to construct multiyear IG wave time series (Figure 4).

We calculated favored wave paths and expected travel times for the IG waves from the Lucky Strike site using shallow water equations implemented in the Cornell Multigrid Coupled Tsunami (COMCOT) modeling package [*Liu et al.*, 1998]. The shallow water equations overestimate velocities (underestimate travel times) in regions where the ocean depth is greater than the IG wavelength. The error is largest at the highest fre-quencies, where the waves are shortest: at our upper frequency limit of 0.01 Hz the calculated wave veloc-ities will be nearly 50% too fast at 5000 m water depth and 30% too fast at 4000 m water depth. This effect is, however, small compared to the 6 h granularity of our data set. For paths entirely in the North Atlantic Ocean, waves spend less than 3 h in deep (>4000 m) water and so the maximum error is less than 1.5 h. For paths starting in the South Atlantic and southern Oceans, the error could be up to 6 h, which is still much narrower than the correlation peaks (supporting information Figure S1). The ray curvature will also be smaller at high frequencies in deep water than that calculated using the COMCOT code: we address possi-ble consequences in section 4.

Table 1. Seafloor Pressure Sensor Sites Used in This Paper

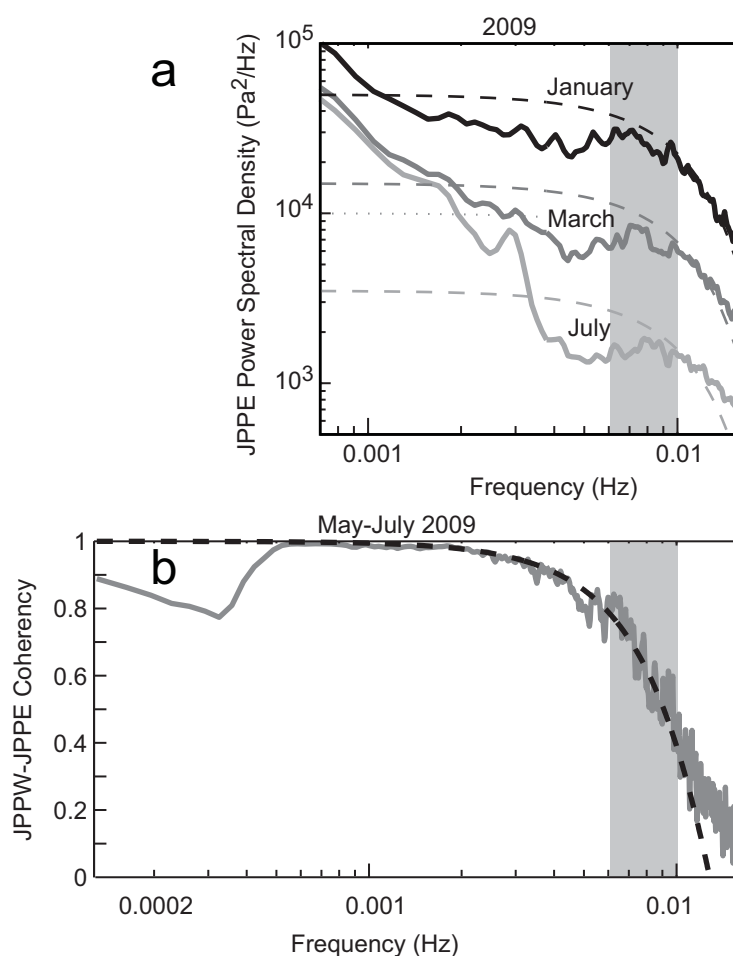| Name	Lat (N)	Lon (E)	Region	Pressure Sensor	Dates
Lucky Strike	37.2°	−32.3°	Central North Atlantic Ocean	Seabird SBE53	Aug 2008–May 2013
DART 44401	37.5°	−50.0°	West North Atlantic Ocean	DART gen. II	Aug 2007–May 2010
DART 44402	38.2°	−67.9°	Westernmost North Atlantic Ocean	DART gen. II	Aug 2007–Jan 2008
DART 42407	15.3°	−68.2°	Gulf of Mexico	DART gen. II	Apr 2006–May 2008

Figure 3. Lucky Strike site seafloor pressure spectra and coherency between two nearby gauges. The frequency band we use to calculate IG wave energy (0.006–0.01 Hz) is highlighted in gray. (a) Pressure spectra averaged over 1 month in different seasons. Solid lines = data; dashed lines = expected shape due to pressure attenuation with depth, assuming a flat sea-surface spectra. (b) Coherency between two gauges separated by 3180 m horizontally. Solid line = measured values and dashed line = predicted values using *Webb* [1986].

We calculated wave amplitudes as a function of time starting from a 2-D Gaussian source with 10 cm amplitude and 0.18° standard deviation, located over the Lucky Strike measurement site. By reciprocity [e.g., *Korolev*, 2011], regions of the ocean that receive the highest amplitudes from this source should also be the most efficient at propagating IG wave energy to the measurement site. Reciprocity requires that the propagation is linear, which is valid for the small amplitudes of IG waves compared to their wavelength. For the Lucky Strike site, the most favorable regions for the propagation of IG waves are to the northeast (toward the British islands) and the southwest (toward Guyana-Venezuela) (Figure 5a).

We calculated the correlation coefficient r [*Pearson*, 1895] between the measured deep ocean IG waves and $H_S * T_p^2$ at each point in our map domain, using 30 day (120 pt) time series centered on the target day. We also calculated the probability of no correlation for each value using the student's t test. The window length of 30 days generally spans at least two weather fronts, providing higher correlation reliability than do shorter windows. We calculated the correlation between $H_S * T_p^2$ and the sea surface IG wave signal in meters, which corresponds to the formulation provided by *Ardhuin et al.* [2014].

We select the correlation coefficient whose time lag from the source site is closest to the expected delay for the propagation of IG waves between the source and the seafloor site. For the Lucky Strike seafloor site, we used the travel times estimated using the COMCOT code (Figure 5b). The results are not significantly different from results calculated assuming a lag of 4 h everywhere and so we used a lag of 4 h everywhere for the DART sites.
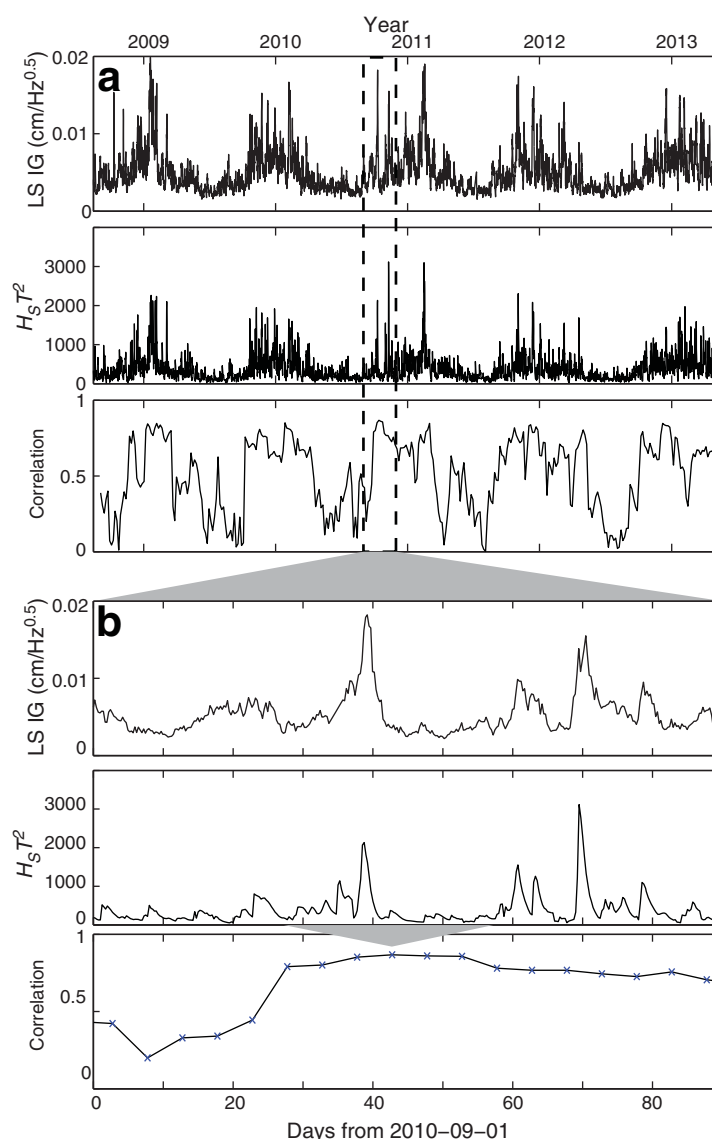
Figure 4. Example of data and correlations. (a) All dates in the Lucky Strike data set. (b) Zoom on 90 days in 2009. (top) Lucky Strike IG wave levels. (middle) $H_S * T_P^2$ levels at 35°N, 10°W. (bottom) Correlation between the two using a 30 day window. The 30 day window corresponding to one correlation value is indicated in Figure 4b by the gray triangle between the middle and bottom windows.

We generally interpret a significant and high correlation coefficient between the IG wave generation parameter in a given region and the IG waves measured at the deep ocean site (at a delay corresponding to the IG wave propagation time between the region and the site) as indicating that the region is a source for the observed deep ocean IG waves. However, some factors could generate "false positives" (high correlation without causation) or "false negatives" (low or insignificant correlation despite causation). First, the long-period wave groups associated with a strong IG wave generation parameter are generally spread out over a large section of ocean, potentially indicating a much larger "source region" than is true (or even multiple separate source regions if the wavefront touches different coasts at the same time). Second, errors in calculated propagation times could change the region with the highest correlation coefficient. A false negative may be created if the IG wave generating signal is masked by a second signal, such as local trade winds.

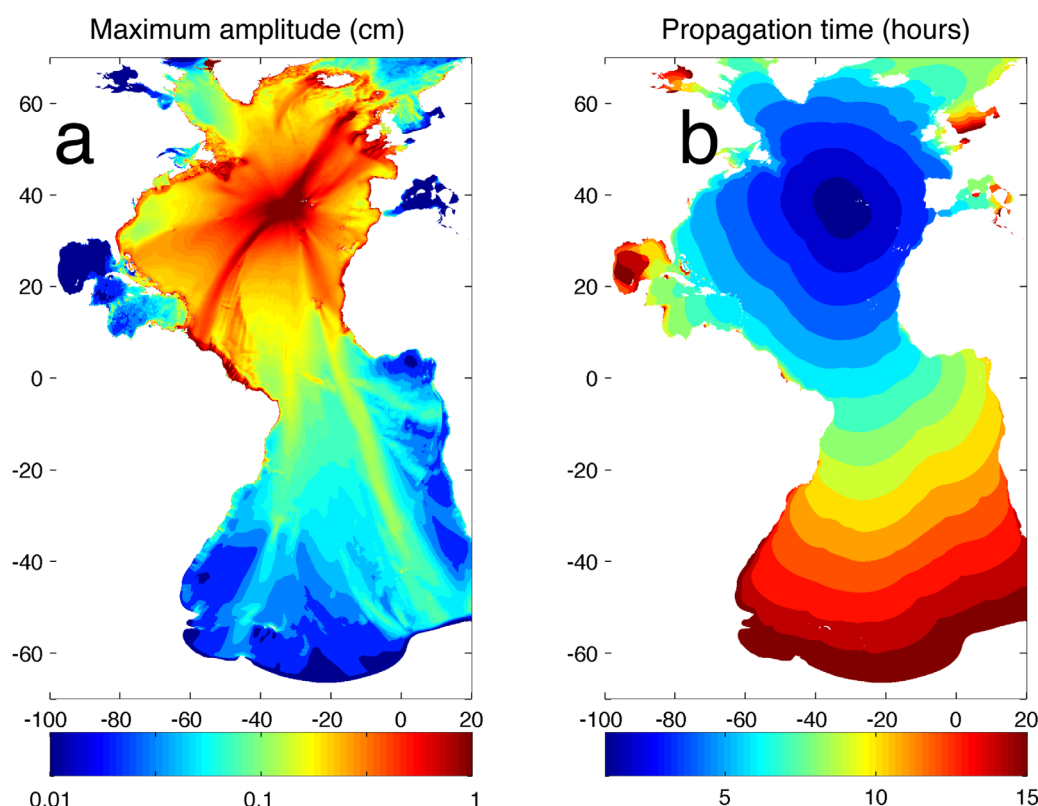To investigate the importance of these factors, we analyzed supporting information data, including the effect of changes in the correlation delay on the position and shape of the high-correlation regions, and spatial variations in the wave directional spread and peak period (which can indicate whether there is a local trade wind effect). We generally average correlations over several months to remove random high-correlation episodes and we discard regions whose correlations have less than a 95% probability of significance more than 25% of the time during the strong source wave season (or 50% of the time, for averages over all seasons).

We tested the effect of allowing up to 48 h of time lag (positive and negative) between the IG wave generation parameter and deep ocean sites on the maximum correlations: allowing such a range increases the size of the correlated regions, mostly in the offshore direction from which the source waves came, indicating that the parameters of the source waves are developed well before they reach shore. The latitude ranges of the sources do not significantly change, however, indicating that errors in the propagation times for IG waves do not strongly affect the results (see supporting information for figures).

Figure 5. Wave propagation time and preferred directions for the Lucky Strike site. (a) Amplitudes of waves propagating from a small isotropic source with magnitude and wavelength consistent with IG waves over the Lucky Strike site: by reciprocity the regions with the highest amplitudes should also generate the highest amplitude to the Lucky Strike site for a given source signal. (b) Propagation times from/to the Lucky Strike site (hours).

We also calculated wave directional spreads and T_P over the study region. Regions with anomalously high spread and low T_P may be affected by local winds that will modify the IG wave generation parameter and could therefore create a false negative.

3. Results

3.1. Lucky Strike Site

The strongest $H_S * T_p^2$ values are at the highest latitudes on the east side of the ocean basins (Figure 6a). In the Northern Hemisphere, $H_S * T_p^2$ is strongest in the northeast Atlantic Ocean, particularly off the coast of Ireland and at the entrance to the North Sea. In the southern Atlantic, $H_S * T_p^2$ is strongest near the southern tip of Africa. The stronger $H_S * T_p^2$ on the eastern edge of the ocean basin reflects the dominant propagation of storms from west to east, increasing both wave amplitude and dominant period to the east.

The strongest correlations between $H_S * T_p^2$ values and the Lucky Strike IG wave signal are not at the high latitudes where $H_S * T_p^2$ is strongest, but rather at midlatitudes off of the west coasts of southern Europe and northern Africa (Figure 6b). The correlations with this region are highest (>0.7) in northern hemisphere winter (Figure 6b, middle) and insignificant in northern hemisphere summer (Figure 6b, right). In northern hemisphere summer, the correlations are highest around the Gulf of Guinea ($-15°$S to $0°$S on the African coast). No other area has as high a correlation as these regions, which we refer to hereafter as the "primary" and "secondary" IG wave source regions, respectively.

Although both of the source regions are on the east side of the Atlantic Ocean basin, neither is in a region of particularly strong $H_S * T_p^2$. In fact, the Gulf of Guinea has some of the lowest average $H_S * T_p^2$ values observed on the east side of the Atlantic Ocean (Figure 6). In addition, both of these regions have weak IG wave propagation paths toward the Lucky Strike site (Figure 5a).
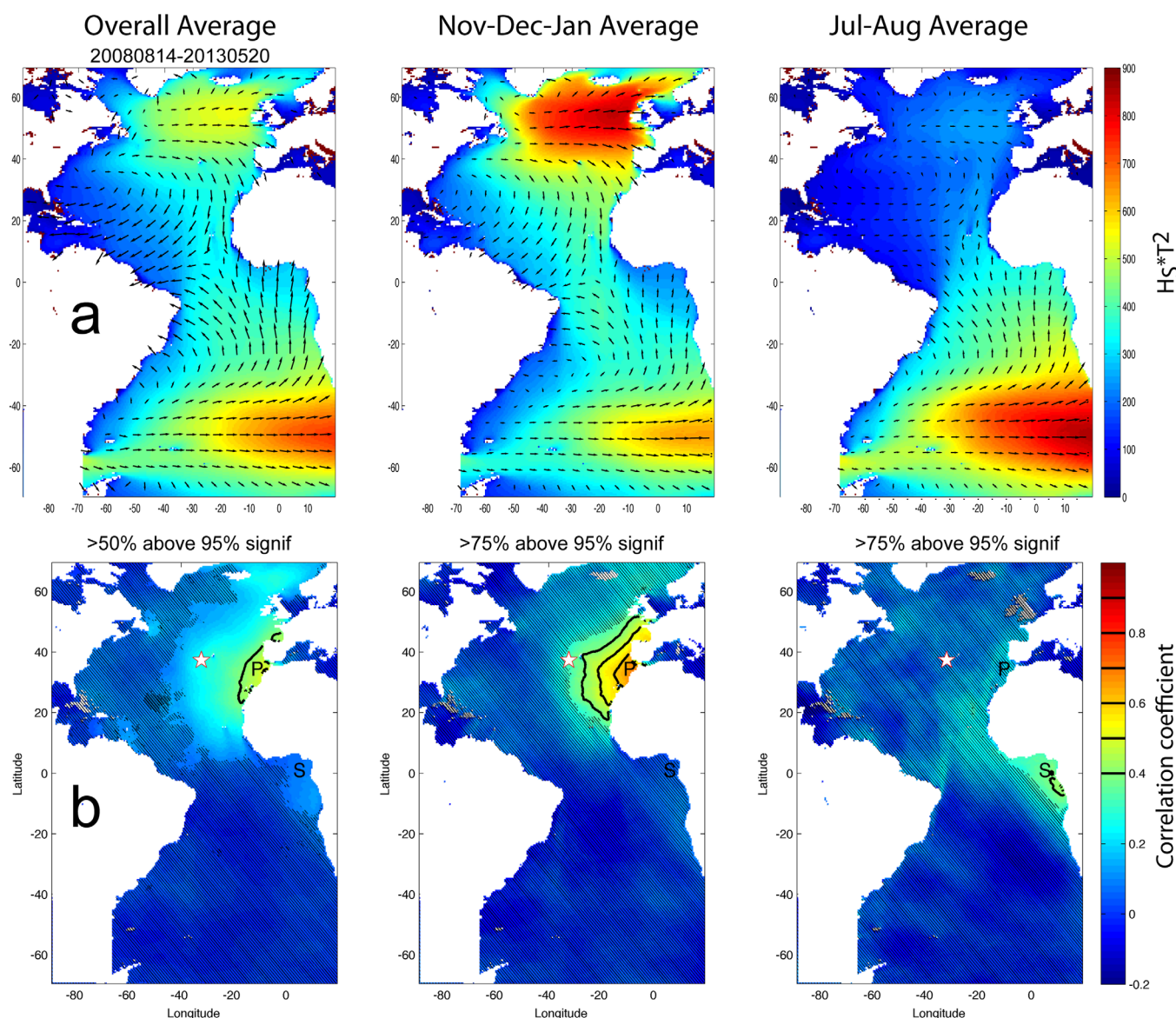
Figure 6. Infragravity wave generation parameters and their correlation with Lucky Strike IG wave levels. (left) All dates. (middle) "Winter" months with best correlations (November, December, and January). (right) Summer months with best correlations (July and August). (a) Averaged generation parameter ($H_S * T_P^2$) levels (colors) and dominant wave directions (arrows). (b) Average correlations. Values above 0.4 are contoured every 0.1, and correlations with less than 95% probability of being significant are hatched. Star shows the seafloor measurement site. "P" and "S" mark the primary and secondary sources, respectively.

Both of these regions are swept by swells travelling eastward from higher latitudes. These swells also strike the west coast of Africa, but the correlation coefficient is significantly lower there, especially between about 5°N and 20°N. This region has relatively strong local trade winds, so that one may wonder if locally generated high-frequency waves could mask the signal from longer waves travelling eastward from higher latitudes. Although the wave directional spread is relatively high in this region (supporting information Figure S3), T_P is also high (more than 12 s, supporting information Figure S4), indicating that trade winds do not dominate the sea state.

The East Atlantic margin north of 50°N, which has the strongest IG wave generation parameters (Figure 6b) as well as a favorable wave propagation path to Lucky Strike (Figure 5a), has a much weaker correlation coefficient that the lower latitude primary IG wave source region.

Although the South Europe/North Africa and Gulf of Guinea regions consistently dominate the correlation with the Lucky Strike site in their strong seasons, there were other short-term correlation peaks during the

5 year data span, most commonly in the Northeast Atlantic and in the Guyana-Caribbean region. The correlation peaks correspond to particularly strong source parameters, notably category 3–4 hurricanes for the western Atlantic peaks. A video of the correlations and $H_S * T_p^2$ over time can be found in supporting information.

3.2. DART Buoy Sites

We evaluated 3 years of IG wave energy at site DART 44401. This site shows very similar correlation pattern to the Lucky Strike site, with strong correlation with the primary IG wave source region in Northern Hemisphere winter and a small correlation with the secondary IG wave source in Northern Hemisphere summer (Figure 7a). This site is located 1600 km west of the Lucky Strike site: the similarity of the correlation suggests that the primary and secondary IG wave source regions are the same for a large portion of the North Atlantic Ocean.

We only have 4 months of data from DART 44402, located 1600 km west of DART 44401, near the edge of the North American continental slope. The data span the period from 28 August 2007 to 5 January 2008: which is not ideal for evaluating the correlation with the primary source region and is useless for evaluating the correlation with the secondary source region. Two large circular regions in the central and western North Atlantic Ocean dominate the correlations (Figure 7b). These regions hosted two strong storms during the measurement period, but no such correlation peaks are seen during the same time span at DART site 44401. The close proximity of DART 44402 to the U.S. continental shelf may influences its IG wave sources: we note that the HEBBLE site—which had a highly variable IG wave level [*Webb et al.*, 1991]—is also close to this continental shelf (Figure 1). Although IG waves over DART 44402 appear to be mostly sensitive to local sea states, they also have a significant correlation with the "primary" source. The correlation increases at the beginning of Northern Hemisphere winter, although the data do not cover the month span (1 November to 31 January) that we used to calculate the average correlations at the other sites.

We have 16 months of data from DART 42407, located in the Caribbean Sea. The IG waves measured there are mostly correlated with regions in the Caribbean Sea and nearby western North Atlantic Ocean (Figure 7c), indicating that this site has different IG wave source regions than do the North Atlantic sites. The Lesser and Greater Antilles island arcs appear to act as efficient barriers for the propagation of IG wave energy into and out of the Caribbean Sea, as shown by *Rawat et al.* [2014]. This can also be seen in our IG wave propagation model (Figure 5a).

4. Discussion

4.1. Source Regions for IG Waves

Our analysis reveals two principal source regions for IG waves at our deep North Atlantic Ocean sites: (1) a primary (winter) source on the western coasts of southern Europe and northwest Africa, and (2) a secondary (summer) source in the region of the Gulf of Guinea. The actual source region may be smaller than the regions with a high-correlation coefficient (Figure 6b) as the correlations are associated with sources whose spatial dimensions are on the order of 10°. Although the deep ocean sites span a limited part of the North Atlantic Ocean (Figure 1), the relatively weak propagation pathways from the identified source regions suggest that there are probably not other important deep ocean IG wave sources that are hidden from these sites.

Rawat et al. [2014] modeled deep ocean IG waves corresponding to the strongest deep ocean IG waves observed in the North Atlantic Ocean in winter 2007–2008. These waves were generated by a storm within the primary source region, although there were several storms with stronger IG wave generation parameters at higher latitudes. The fact that none of these storms generated as strong a deep ocean IG wave peak in the North Atlantic supports our correlation-based identification of the primary source region.

The shape and maximum correlation coefficient of the source region around the Gulf of Guinea region is probably biased by the highly variable efficiency of IG wave propagation from this region to the North Atlantic: the spot showing with the highest correlation with the Lucky Strike data (just south of Cape Lopez at 1°S, Figure 6b) also has the most efficient propagation path to that site (Figure 5a). Ray tracing using velocities calculated from the full wave equation show that the difference in propagation efficiency is even stronger at the highest frequencies, for which there is less refraction toward the coasts of the northern part of the Gulf of Guinea. A stronger source to the south or north could simply be masked by the weaker IG
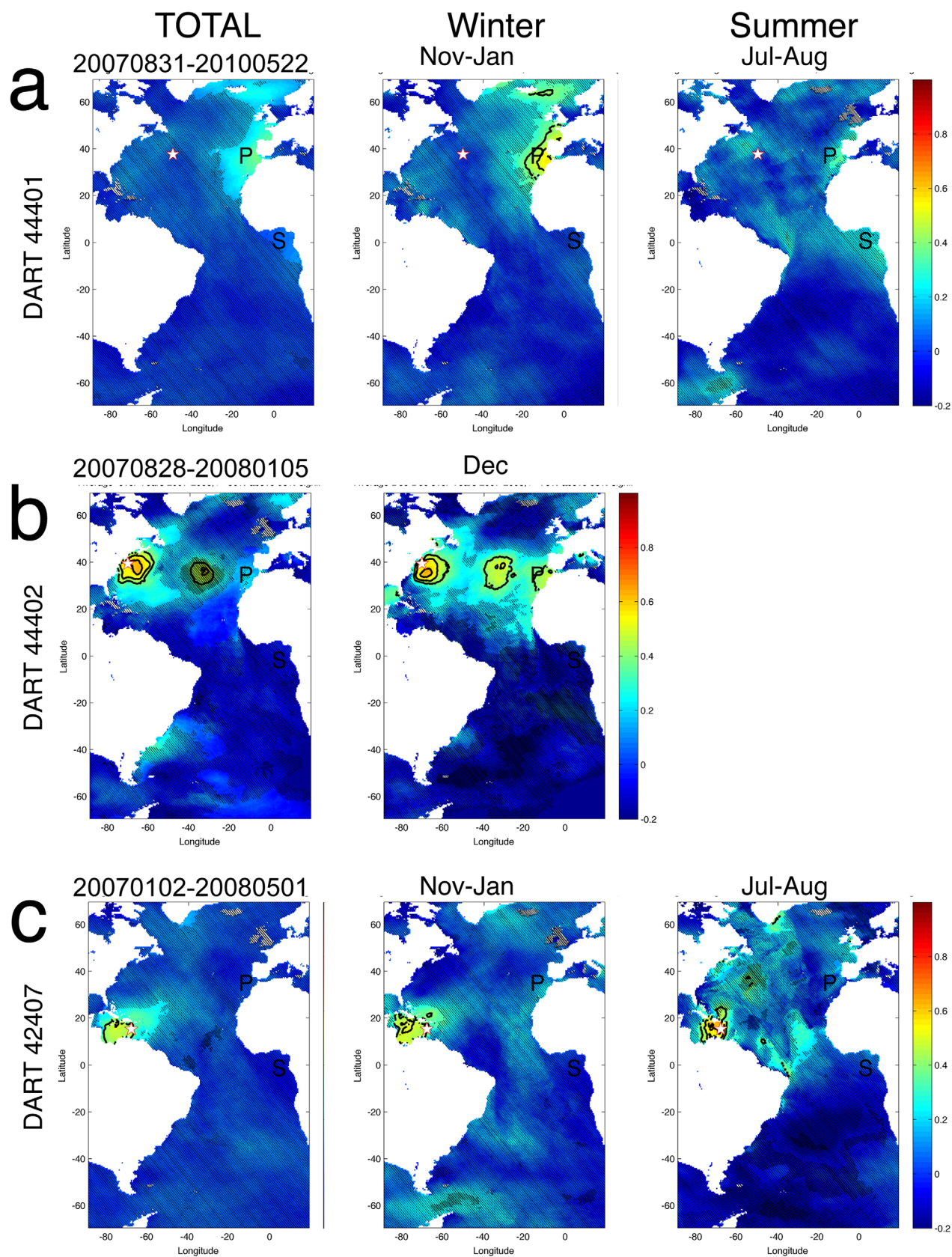
Figure 7.

wave propagation from these regions. A deep ocean IG wave measurement site (or sites) in the South Atlantic Ocean would greatly help to refine the location of this source.

Why are southern Europe/northwest Africa and the Gulf of Guinea the dominant sources of IG wave energy in the deep Northern Atlantic Ocean? Although both source regions are on the eastern boundary of the Atlantic Ocean, where $H_S * T_P^2$ values are generally strongest, they have some of the lowest $H_S * T_P^2$ values along this boundary. Also, neither of these regions has a favorable IG wave propagation path to the Lucky Strike site. *Raubenheimer and Guza* [1996] observed that the amount of IG waves generated for a given impinging wave height varies significantly between sites (and is fairly constant at a given site): it appears that the morphology or orientation of the source sites are more important for generating deep ocean IG waves than is the amplitude of the IG wave generation parameter.

4.2. Possible Links With Seismic Noise

Both regions may also be source regions for low-frequency energy observed by global seismological stations. The primary source region has been suggested as a source for background-free oscillations of the earth between 0.002 and 0.03 Hz (the earth's "hum") based on correlations with H_S [*Traer et al.*, 2012], whereas the secondary source region also contains the source region of a 26 s (0.038 Hz) peak in "microseismic" Rayleigh wave oscillations [*Holcomb*, 1980; *Shapiro et al.*, 2006]. It has been suggested that similar ocean wave processes generate the earth's hum and IG waves [*Webb*, 2007; *Uchiyama and McWilliams*, 2008; *Webb*, 2008; *Ardhuin et al.*, 2015] and the concurrence of the source regions supports this hypothesis.

Ardhuin et al. [2015] recently reproduced the spatial and temporal variability of the earth's hum to within an order of magnitude using *Hasselmann*'s [1963] theory for the generation of seismic waves by ocean waves over a sloping bottom. They deliberately ignore regional variations in structure/coupling, assuming that the hum levels depend solely on coastal ocean wave characteristics. There is, however, significant room for improving the fit of the model to the data, and one possibility is to evaluate the effect of including regional variations in structure and/or coupling.

4.3. Characteristics of the Source Regions

What characteristics of these regions favor IG wave generation or leakage? Our data do not answer this question, and bathymetric data are not precise enough around the ocean basin to fully evaluate morphological effects, but we will summarize theories for the generation and leakage of IG waves at/from coastlines and discuss which favorable factors may be found in the source regions.

Previous studies of IG waves have suggested that the seafloor morphology and the direction of impinging waves influence the generation and leakage of IG waves. *Herbers et al.* [1995a] demonstrated that the amount of energy generated depends not only on the amplitudes but also on the angles and frequencies of the impinging waves. Variations in the very nearshore depth profiles can also have a strong effect on IG wave generation, as is seen in the tidal modulation of IG wave generation presumed to be the result of a change from a convex beach profile at low tides to a concave profile at high tides [*Thomson et al.*, 2006]. Once generated, IG waves tend to leak more to the open ocean if the continental shelf is absent or narrow [*Herbers et al.*, 1995b] and/or if there are alongshore variations in the coastal depth profile [*van Dongeren and Svendsen*, 2000; *Thomson et al.*, 2007]. In addition, laboratory experiments showed that IG waves may break and dissipate over gently sloping bottoms [*van Dongeren et al.*, 2007].

The leakage of IG waves is also controlled by wave obliquity with respect to the shore. *Reniers et al.* [2002] suggested that outgoing IG waves may be refractively trapped if incident wave groups are sufficiently oblique. *Herbers et al.* [1995a] showed that such a refractive trapping was stronger for directionally broad short waves. As a synthesis of these previous findings, conditions promoting the leakage of IG waves include: (1) shore-normal narrow banded incident short waves; (2) narrow continental shelves and steep beaches. The former condition requires that the IG waves source site is located at distance from the fetches, which is the case for the two regions that we identified. These two regions also receive shore-normal waves (Figure 6a) with small-wave directional spread (the spread is particularly small around the Gulf of Guinea, supporting information Figure S3). Finally, the regions are bounded by

Figure 7. Average correlations at other seafloor sites. Contouring and hatching as in Figure 6. The star indicates the seafloor site location. (a) DART 44401. (b) DART 44402. (c) DART 42407. (left column) Average over all data. (middle column) Average over "winter" months with best correlations. (right column) Average over summer months with best correlations.

narrow continental shelves (40–60 km) and their beaches often have steep upper parts, such as in Central Portugal (slope up to 0.12) [*Dodet et al.*, 2013], Northern Morocco (slope of 0.03 to 0.08) [*Hakkou et al.*, 2011], and the Gulf of Guinea [*Allersma and Tilmans*, 1993]. The occurrence of steep beaches is partly due to the presence of small to moderate tidal ranges, which controls the overall beach morphology, together with the sediment diameter and H_S [*Masselink and Short*, 1993]. These small to moderate tidal ranges are associated with their narrow continental shelves, which limits tidal amplification through shoaling and resonance.

Even if conditions (1) and (2) are necessary for a site to be a good source for deep ocean IG waves, they may not be sufficient and other smaller-scale features may be relevant. For example, the western coast of Ireland does not appear to be a good source for deep ocean IG waves even though it faces the highest $H_s*T_p^2$ in the North Atlantic, the waves arrive shore normally and the shelf width and tidal ranges are moderate. A possible explanation could be the very irregular rocky coastline in this region, with alternating embayed beaches, rias, and cliffs. This morphological setting may promote the trapping and/or dissipation of IG waves, although this hypothesis needs to be verified through detailed studies. The wave directional spread there is also higher than in the source regions.

Although the above factors may favor the creation and leakage of IG waves in each region, they are not completely unique to these regions and very local structures may be the key to the domination of these sites in creating both IG waves and seismic noise. More detailed studies of IG wave generation in these regions should allow a more precise location of the source regions, and detailed studies of the morphology of these regions may reveal key processes in the generation and leakage of IG wave energy.

This study reveals that there are well-defined regions for the generation of deep ocean IG waves observed in the North Atlantic Ocean, that these regions are coastal, and that they depend on the coastal morphology (and perhaps exposure to narrow wave directional spread energy from storms) rather than the level of ocean wave energy. We expect the same to be true for other ocean basins, which could be confirmed by a follow-up study using pressure data from DART buoys (of which there are many in the Pacific and some in the Indian ocean) or long-term broadband Ocean Bottom Seismometer (using a differential or absolute pressure gauge as the pressure sensor) or geodesy (absolute pressure gauge) studies. There are no DART buoys in the South Atlantic Ocean: a long-term IG wave study there would be very useful for determining the extent and strength of the Gulf of Guinea source.

5. Conclusions

Deep ocean IG waves observed in the North Atlantic Ocean come primarily from two sources: (1) a "primary" source region on the eastern margin of the North Atlantic Ocean, from the northern end of the Iberian peninsula to the westernmost point of West Africa; and (2) a "secondary" source region around the Gulf of Guinea. The first source is primarily active in Northern Hemisphere winter whereas the second is active in Southern Hemisphere winter. The source regions have relatively weak IG wave generation parameters (significant wave height multiplied by the wave period squared), indicating that the dominant factor in generating deep ocean IG waves is the coastal morphology or incident wave direction/spread rather than the wave height and period. These regions may also be the sources of seismological noise observed on global seismological station, consistent with recent studies indicating that ocean waves are important in generating background seismological noise.

Possible factors behind the generation of deep ocean IG waves in these regions may be the relatively narrow (40–60 km) continental shelf and steep upper beach parts in both regions, as well as swell arriving perpendicular to the beach with small-wave directional spread. Very local bathymetric variations may also play an important role and should be investigated.

References

Allersma, E., and W. M. K. Tilmans (1993), Coastal conditions in West Africa: A review, *Ocean Coastal Manage.*, *19*, 199–240.
Apel, J. R. (1987), *Principles of Ocean Physics*, Academic, London, U. K.
Ardhuin, F., and T. H. C. Herbers (2013), Noise generation in the solid earth, oceans and atmosphere, from nonlinear interacting surface gravity waves in finite depth, *J. Fluid Mech.*, *716*, 316–348, doi:10.1017/jfm.2012.548.

Ardhuin, F., A. Rawat and J. Aucan (2014), A numerical model for free infragravity waves: Definition and validation at regional and global scales, *Ocean Modell.*, *77*, 20–32, doi:10.1016/j.ocemod.2014.02.006.

Ardhuin, F., L. Gualtieri, and E. Stutzmann (2015), How ocean waves rock the Earth: Two mechanisms explain microseisms with periods 3 to 300 s, *Geophys. Res. Lett.*, *42*, 765–772, doi:10.1002/2014GL062782.

Aucan, J., and F. Ardhuin (2013), Infragravity waves in the deep ocean: An upward revision, *Geophys. Res. Lett.*, *40*, 3435–3439, doi:10.1002/grl.50321.

Baldock, T. E. (2012), Dissipation of incident forced long waves in the surf zone—Implications for the concept of "bound" wave release at short wave breaking, *Coastal Eng.*, *60*, 276–285.

Ballu, V., et al. (2009), A seafloor experiment to monitor vertical deformation at the Lucky Strike volcano, Mid-Atlantic Ridge, *J. Geod.*, *83*(2), 147–159, doi:10.1007/s00190-008-0248-3.

Bertin, X., E. Prouteau, and C. Letetrel (2013), A significant increase in wave height in the North Atlantic Ocean over the 20th century, *Global Planet. Change*, *106*, 77–83, doi:10.1016/j.gloplacha.2013.03.009.

Bidlot, J. R., P. A. E. M. Janssen, and S. Abdalla (2007), A revised formulation for ocean wave dissipation and its model impact, *Tech. Memo. 509*, 29 pp., European Centre for Medium-Range Weather Forecasts (ECMRWF), Reading, U. K.

Bromirski, P. D., O. V. Sergienko, and D. R. MacAyeal (2010), Transoceanic infragravity waves impacting Antarctic ice shelves, *Geophys. Res. Lett.*, *37*, L02502, doi:10.1029/2009GL041488.

Cannat, M., et al. (2011), *MoMar-Demo at Lucky Strike. A near-real time multidisciplinary observatory of hydrothermal processes and ecosystems at the Mid-Atlantic Ridge, Abstract OS22A-05 presented at 2011 Fall Meeting*, AGU, San Francisco, Calif.

Colaço, A., et al. (2011), MoMAR-D: A technological challenge to monitor the dynamics of the Lucky Strike vent ecosystem, *ICES J. Mar. Sci.*, *68*(2), 416–424, doi:10.1093/icesjms/fsq075.

Crawford, W. C., S. C. Webb, and J. A. Hildebrand (1991), Seafloor compliance observed by long-period pressure and displacement measurements, *J. Geophys. Res.*, *96*(10), 16,151–16,160.

Dee, D. P., et al. (2011), The ERA-Interim reanalysis: Configuration and performance of the data assimilation system, *Q. J. R. Meteorol. Soc.*, *137*(656), 553–597, doi:10.1002/qj.v137.656.

Dodet, G., X. Bertin, and R. Taborda (2010), Wave climate variability in the North-East Atlantic Ocean over the last six decades, *Ocean Modell.*, *31*(3–4), 120–131, doi:10.1016/j.ocemod.2009.10.010.

Dodet, G., X. Bertin, N. Bruneau, A. B. Fortunato, A. Nahon, and A. Roland (2013), Wave-current interactions in a wave-dominated tidal inlet, *J. Geophys. Res. Oceans*, *118*, 1587–1605, doi:10.1002/jgrc.20146.

Dolenc, D., B. Romanowicz, P. McGill, and W. S. D. Wilcock (2008), Observations of infragravity waves at the ocean-bottom broadband seismic stations Endeavour (KEBB) and Explorer (KXBB), *Geochem. Geophys. Geosyst.*, *9*, Q05007, doi:10.1029/2008GC001942.

Fukao, Y., K. Nishida, and N. Kobayashi (2010), Seafloor topography, ocean infragravity waves, and background Love and Rayleigh waves, *J. Geophys. Res.*, *115*, B04302, doi:10.1029/2009JB006678.

Gallagher, B. (1971), Generation of surf beat by non-linear wave interactions, *J. Fluid Mech.*, *49*(1), 1–20.

Hakkou, M., B. Castelle, A. Benmohammadi, and B. Zourarah (2011), Wae climate and morphosedimentary characteristics of the Kenitrae-Bouknadel sandy coast, Morocco, *Environ. Earth Sci.*, *64*, 1729–1739.

Hasselmann, K. (1962), On the non-linear energy transfer in a gravity-wave spectrum, *J. Fluid Mech.*, *12*(4), 481–500.

Hasselmann, K. (1963), A statistical analysis of the generation of microseisms, *Rev. Geophys.*, *1*(2), 177–210.

Herbers, T. H. C., S. Elgar, and R. T. Guza (1995a), Generation and propagation of infragravity waves, *J. Geophys. Res.*, *100*(C12), 24,863–24,872.

Herbers, T. H. C., S. Elgar, R. T. Guza, and W. C. O'Reilly (1995b), Infragravity-frequency (0.005-0.05 Hz) motions on the shelf. Part II: Free waves, *J. Phys. Oceanogr.*, *25*, 1063–1079.

Holcomb, L. G. (1980), Microseisms: A twenty-six-second spectral line in long-period earth motion, *Bull. Seismol. Soc. Am.*, *70*(4), 1055–1070.

Korolev, Y. P. (2011), An approximate method of short-term tsunami forecast and the hindcasting of some recent events, *Nat. Hazards Earth Syst. Sci.*, *11*(11), 3081–3091, doi:10.5194/nhess-11-3081-2011.

Liu, P. L. F., S. B. Woo, and Y. S. Cho (1998), *Computer Programs for Tsunami Propagation and Inundation*, 104 pp., Cornell Univ., Ithaca, N. Y.

Longuet-Higgins, M. S., and R. W. Stewart (1962), Radiation stress and mass transport in gravity waves, with application to 'surf beats', *J. Fluid Mech.*, *13*(4), 481–504.

Masselink, G., and A. D. Short (1993), The effect of tide range on beach morphodynamics and norphology—A conceptual beach model, *J. Coastal Res.*, *9*(3), 785–800.

Munk, W., F. Snodgrass, and F. Gilbert (1964), Long waves on the continental shelf: An experiment to separate trapped and leaky modes, *J. Fluid Mech.*, *20*(4), 529–554.

Okihiro, M., R. T. Guza, and R. J. Seymour (1992), Bound infragravity waves, *J. Geophys. Res.*, *97*(C7), 11,453–11,469.

Okihiro, M., R. T. Guza, and R. J. Seymour (1993), Excitation of seiche observed in a small harbor, *J. Geophys. Res.*, *98*(C10), 18201–18211.

Pearson, K. (1895), Note on regression and inheritance in the case of two parents, *Proc. R. Soc. London*, *58*(347–352), 240–242.

Pomeroy, A., R. Lowe, G. Symonds, A. R. van Dongeren, and C. Moore (2012), The dynamics of infragravity wave transformation over a fringing reef, *J. Geophys. Res.*, *117*, C11022, doi:10.1029/2012JC008310.

Rabinovich, A. B. (2009), Seiches and harbour oscillations, Handbook of coastal and ocean engineering, *World Scientific Publ.*, 193–236, Singapore.

Rascle, N., and F. Ardhuin (2013), A global wave parameter database for geophysical applications. Part 2: Model validation with improved source term parameterization, *Ocean Modell.*, *70*, 174–188, doi:10.1016/j.ocemod.2012.12.001.

Rascle, N., F. Ardhuin, P. Queffeulou, and D. Croizé-Fillon (2008), A global wave parameter database for geophysical applications. Part 1: Wave-current–turbulence interaction parameters for the open ocean based on traditional parameterizations, *Ocean Modell.*, *25*(3), 154–171.

Raubenheimer, B., and R. T. Guza (1996), Observations and predictions of run-up, *J. Geophys. Res.*, *101*(C11), 25,575–25,587.

Rawat, A. (2015), *Numerical modelling of infragravity waves, PhD thesis*, 127 pp., Univ. Bretagne Occidentale, Brest, France.

Rawat, A., F. Ardhuin, V. Ballu, W. Crawford, C. Corela, and J. Aucan (2014), Infragravity waves across the oceans, *Geophys. Res. Lett.*, *41*, 7957–7963, doi:10.1002/2014GL061604.

Reniers, A. J. H. M., A. R. van Dongeren, J. A. Battjes, and E. B. Thornton (2002), Linear modeling of infragravity waves during Delilah, *J. Geophys. Res.*, *107*(C10), 3137, doi:10.1029/2001JC001083.

Rhie, J., and B. Romanowicz (2006), A study of the relation between ocean storms and the Earth's hum, *Geochem. Geophys. Geosyst.*, *7*, Q10004, doi:10.1029/2006GC001274.

Shapiro, N. M., M. H. Ritzwoller, and G. D. Bensen (2006), Source location of the 26 sec microseism from cross-correlations of ambient seismic noise, *Geophys. Res. Lett.*, *33*, L18310, doi:10.1029/2006GL027010.

Shillington, F. A. (1981), Low frequency 0.045-Hz swell from the southern ocean, *Nature*, *290*(5802), 123–125.

Snodgrass, F. E., G. W. Groves, K. F. Hasselmann, G. R. Miller, W. H. Munk, and W. H. Powers (1966), Propagation of ocean swell across the Pacific, *Philos. Trans. R. Soc. London A*, *259*, 432–497.

Symonds, G., D. A. Huntley, and A. J. Bowen (1982), Two-dimensional surfbeat: Longwave generation by a time varying breakpoint, *J. Geophys. Res.*, *87*(C1), 492–298.

Thomson, J., S. Elgar, B. Raubenheimer, T. H. C. Herbers, and R. T. Guza (2006), Tidal modulation of infragravity waves via nonlinear energy losses in the surfzone, *Geophys. Res. Lett.*, *33*, L05601, doi:10.1029/2005GL025514.

Thomson, J., S. Elgar, T. H. C. Herbers, B. Raubenheimer, and R. T. Guza (2007), Refraction and reflection of infragravity waves near submarine canyons, *J. Geophys. Res.*, *112*, C10009, doi:10.1029/2007JC004227.

Tolman, H. L. (2009), User manual and system documentation of WAVEWATCH III[TM] version 3.14, *MMAB Contrib., Tech. Note 276*, 220 pp., NOAA-NWS, Camp Springs.

Traer, J., P. Gerstoft, P. D. Bromirski, and P. M. Shearer (2012), Microseisms and hum from ocean surface gravity waves, *J. Geophys. Res.*, *117*, B11307, doi:10.1029/2012JB009550.

Uchiyama, Y., and J. C. McWilliams (2008), Infragravity waves in the deep ocean: Generation, propagation, and seismic hum excitation, *J. Geophys. Res.*, *113*, C07029, doi:10.1029/2007JC004562.

van Dongeren, A., J. Battjes, T. Janssen, J. van Noorloos, K. Steenhauer, G. Steenbergen, and A. Reniers (2007), Shoaling and shoreline dissipation of low-frequency waves, *J. Geophys. Res.*, *112*, C02011, doi:10.1029/2006JC003701.

van Dongeren, A. R., and I. A. Svendsen (2000), Nonlinear and 3D effects in leaky infragravity waves, *Coastal Eng.*, *41*(4), 467–496.

Webb, S. C. (1986), Coherent pressure fluctuations observed at two sites on the deep sea floor, *Geophys. Res. Lett.*, *13*(1), 141–144.

Webb, S. C. (2007), The Earth's 'hum' is driven by ocean waves over the continental shelves, *Nature*, *445*, 754–756.

Webb, S. C. (2008), The Earth's hum: The excitation of Earth normal modes by ocean waves, *Geophys. J. Int.*, *174*(2), 542–566.

Webb, S. C. and W. C. Crawford (1999), Long period seafloor seismology and deformation under ocean waves, *Bull. Seismol. Soc. Am.*, *89*(6), 1535–1542.

Webb, S. C., X. Zhang and W. C. Crawford (1991), Infragravity waves in the deep ocean, *J. Geophys. Res.*, *96*(C2), 2723–2736.

Yamamoto, T., and T. Torii (1986), Seabed shear modulus profile inversion using surface gravity (water) wave-induced bottom motion, *Geophys. J. R. Astron. Soc.*, *85*(2), 413–431.

Zha, Y., S. C. Webb, S. Nooner and W. C. Crawford (2014), Spatial distribution and temporal evolution of crustal melt distribution beneath the East Pacific Rise at 9°–10°N inferred from 3-D seafloor compliance modeling, *J. Geophys. Res. Solid Earth*, *119*, 4517–4537, doi:10.1002/2014JB011131.